Applied Physics A (2019) 125:193
https://doi.org/10.1007/s00339-019-2487-y

Applied Physics A
Materials Science & Processing

Structural, spectroscopic and dielectric properties of Ca-doped $BaTiO_3$

Mohamed Hassen Khedhri[1] · Najmeddine Abdelmoula[1] · Hamadi Khemakhem[1] · Redouane Douali[2] · Frederic Dubois[2]

Received: 4 January 2019 / Accepted: 7 February 2019 / Published online: 19 February 2019

Abstract
Ca-doped barium titanate $BaTiO_3$ nanopowders were synthesized by the sol–gel process using barium acetate [$Ba(CH_3COO)_2$], calcium acetate [$Ca(CH_3COO)_2$] and titanium butoxide [$Ti(OC_4H_9)_4$] as precursors. This method was adopted because it allows obtaining powders of high purity, chemical homogeneity and fine particle size, and crystallization is possible at very low temperatures (800 °C) compared to that used by the conventional solid-state reaction method. In this study, the characterization of nanopowders and ceramics using X-ray diffraction (XRD), scanning electron microscopy (SEM), photoluminescence (PL), dielectric measurements, FTIR and Raman spectroscopy is carried out. The results revealed that the calcium ion incorporation had significant effect on structural and dielectric properties of barium titanate $BaTiO_3$ (BT). XRD patterns suggested that nanopowders calcined at the temperature of 800 °C during 2 h could be crystallized into perovskite structure, with an average crystallite size in the range of 19.89–25.04 nm. Furthermore, it was observed that the Ca concentration variation affected the emission process with little displacement in the peak position. These results proved the optical band gap reduction by the presence of inter-band electron levels. Finally, the dielectric properties of the prepared samples were measured, revealing that the dielectric permittivity decreased with frequency increase, and the grain size and Curie temperature of the $Ba_{1-x}Ca_xTiO_3$ (BCT) ceramics sintered at 1200 °C were greatly affected by Ca substitution.

1 Introduction

Barium titanate $BaTiO_3$ (BT) is currently one of the most studied ferroelectric compounds [1–4]. Not only does it allow the comprehension of ferroelectric phenomena in a general way, but also it is interesting from the viewpoint of the applications. In fact, it offers a good chemical and mechanical stability, as well as good dielectric properties, thus making it very useful in making transducers and multilayer capacitors in a variety of shapes and sizes.

Barium titanate belongs to the family of perovskites ABO_3, in which A and B are generally metals. It is ferroelectric at room temperature and it is paraelectric beyond the Curie temperature T_C close to 130 °C.

The doping of ferroelectric powders $BaTiO_3$ is of great importance in the fabrication of electrical and electronic devices [1–5] due to intrinsic capacity of the perovskite structure to host ions of different size and the large number of different dopants can be incorporated in the titanate barium (BT) lattice.

The substitution of Ba^{2+} by Ca^{2+} in $BaTiO_3$ leads to the formation of $Ba_{1-x}Ca_xTiO_3$ (BCT) in the tetragonal phase for $x < 0.23$, which shows the solubility limit following the increase in size differences between these two ions (Ba^{2+} and Ca^{2+}). Above this value, a mixture of tetragonal and orthorhombic phases appears up to $x = 0.9$, and, beyond the value, the orthorhombic phase exists.

In the Barium Calcium Titanate system (BCT), the piezoelectric coefficient has been improved from 180 up to 310 pC N^{-1} for $0.02 < x < 0.34$ [6].

This is interesting that other elements, such as Sr^{2+} (BST solution), can replace Ba^{2+} in $BaTiO_3$ to form solid solutions without solubility limits [7]. However, the properties of BCT are better than those obtained in the BST system.

Moreover, calcium incorporation improves the physical properties, especially the stability of the piezoelectric ones, which makes BCT a very useful compound in the creation of

✉ Mohamed Hassen Khedhri
khedhrihassen@yahoo.fr

[1] Laboratory of Multifunctional Materials and Applications (LaMMA), (LR16ES18), Faculty of Sciences of Sfax, University of Sfax, B. P. 1171, 3000 Sfax, Tunisia

[2] Unité de Dynamique et Structure des Matériaux Moléculaires (UDSMM), Université du Littoral Côte d'Opale (ULCO), 62228 Calais, France

electro-optical materials for holographic and photo-refractive applications [8].

In addition, another parameter can significantly influence the physical properties of materials, which is the crystallite size in ceramics. This parameter is directly dependent on the annealing temperature and turns out to be one of the key parameters considerably influencing the dielectric response of the material, such as Curie temperature T_C, physical and structural properties of many compound oxides [9, 10].

On the other hand, several studies [11–14] have shown that the synthesis of ceramics by the traditional solid-state method at temperatures about 1500 °C makes it impossible to obtain crystallites with sizes less than 1 µm.

Furthermore, when the next step is to disperse the nanoparticles in polymer matrices, a fine particle size is required and the sol–gel process is preferable.

In fact, this soft chemistry technique offers us the possibility to obtain powders and ceramics of high purity, good chemical homogeneity and fine particle size at very low temperatures in reference to the classical solid–solid reaction method. On the other hand, the major problem in the nanocrystalline oxide synthesis is the stoichiometry control at the nanoscale level and this is overcome by the sol gel process [11].

To obtain ferroelectric materials with nanoparticle size, we choose the $Ba_{1-x}Ca_xTiO_3$ system with x inferior to 0.2. These nanoparticle compounds were prepared by sol–gel method at low temperature. The structural, spectroscopic and optical properties of Ca-doped $BaTiO_3$ powders were investigated using different techniques such as X-ray diffraction (XRD), FTIR, Raman spectroscopy and photoluminescence analysis. The crystallite size was calculated using Scherrer formula. In addition, the dielectric properties were investigated.

2 Experimental procedure

2.1 Materials and samples preparation

$Ba_{1-x}Ca_xTiO_3$ nanopowders with different Ca concentrations ($x = 0$–0.2) were synthesized by sol–gel process using barium acetate [$Ba(CH_3COO)_2$] (99%, Fluka), calcium acetate [$Ca(CH_3COO)_2$] (99–100%, Aldrich), tetrabutyl titanium [$Ti(C_4H_9O)_4$] (97%, Aldrich), absolute ethanol (C_2H_6O) (99.8%, Aldrich) and acetic acid ($C_2H_4O_2$) (99–100%, Aldrich) as starting chemicals. The pursued synthesis procedure is presented in Fig. 1 and described as follows:

– First, a stoichiometric quantity of $Ti(C_4H_9O)_4$ was dissolved in a mixture of concentrated ethanol and acetic acid with constant stirring using magnetic stirrer for 40 min at room temperature. Subsequently, $Ba(CH_3COO)_2$ and a stoichiometric quantity of $Ca(CH_3COO)_2$ was dissolved in a mixture of acetic acid and deionized water before being heated up to 80 °C.
– Afterwards, the acquired preparation was drizzled slowly into the $Ti(C_4H_9O)_4$ solution and stirred vigorously for approximately 1 h to form a homogeneous solution. 3 h later, a clear gel was formed. The xerogels acquired after this step were dried at 120 °C for 8 h. The xerogels were then calcined at 800 °C for 2 h. This process aimed not only to decompose any organic components formed during the sol–gel process, but also to reach crystalline nanopowder formation (Fig. 1).
– At last, to prepare ceramics, the powders were compressed into discs of 8 mm in diameter and 1 mm in thickness, followed by sintering at 1200 °C for 4 h.

2.2 Characterization

The thermal decomposition of xerogels was studied by means of a TGA 4000 Thermogravimetric Analyzer over the temperature range of 30–800 °C (10 °C/min) and differential scanning calorimeter DSC 4000 (PerkinElmer) over the temperature range of 30–400 °C (10 °C/min) in a dynamic oxygen atmosphere.

The crystal structures of $Ba_{1-x}Ca_xTiO_3$ powders were determined by X-ray diffraction (XRD) using a D8 Advance instrument (Bruker) with the main specifications of $CuK_{\alpha 1}$ radiation ($\lambda = 1.54178$ Å). Lattice parameters were defined by Rietveld refinement using Fullprof program. IR spectra were recorded with an FT-IR spectrometer VERTEX 80 (Bruker) in the 400–4000 cm^{-1} range on as-pressed disks using KBr as the binding material. The Raman spectroscopy data were obtained at room temperature by a system Horiba Jobin Yvon Spectrometer Micro Raman with source laser excitation and detector of 1024 pixels with CCD High sensitivity, mounted in an Olympus microscope BX41TF with spatial resolution < 1 µm.

The photoluminescence (PL) spectra were recorded at room temperature. In PL measurements, the samples were excited at 380 nm. Dielectric constant ε_r for the investigated samples was measured by precise impedance analyzer 4294A (Agilent Technologies) controlled by a computer at 1 kHz over the temperature range from − 150 to 250 °C for the ceramics and in the frequency range from 1 kHz to 1 MHz over the temperature range from room temperature to 250 °C for the nanopowders.

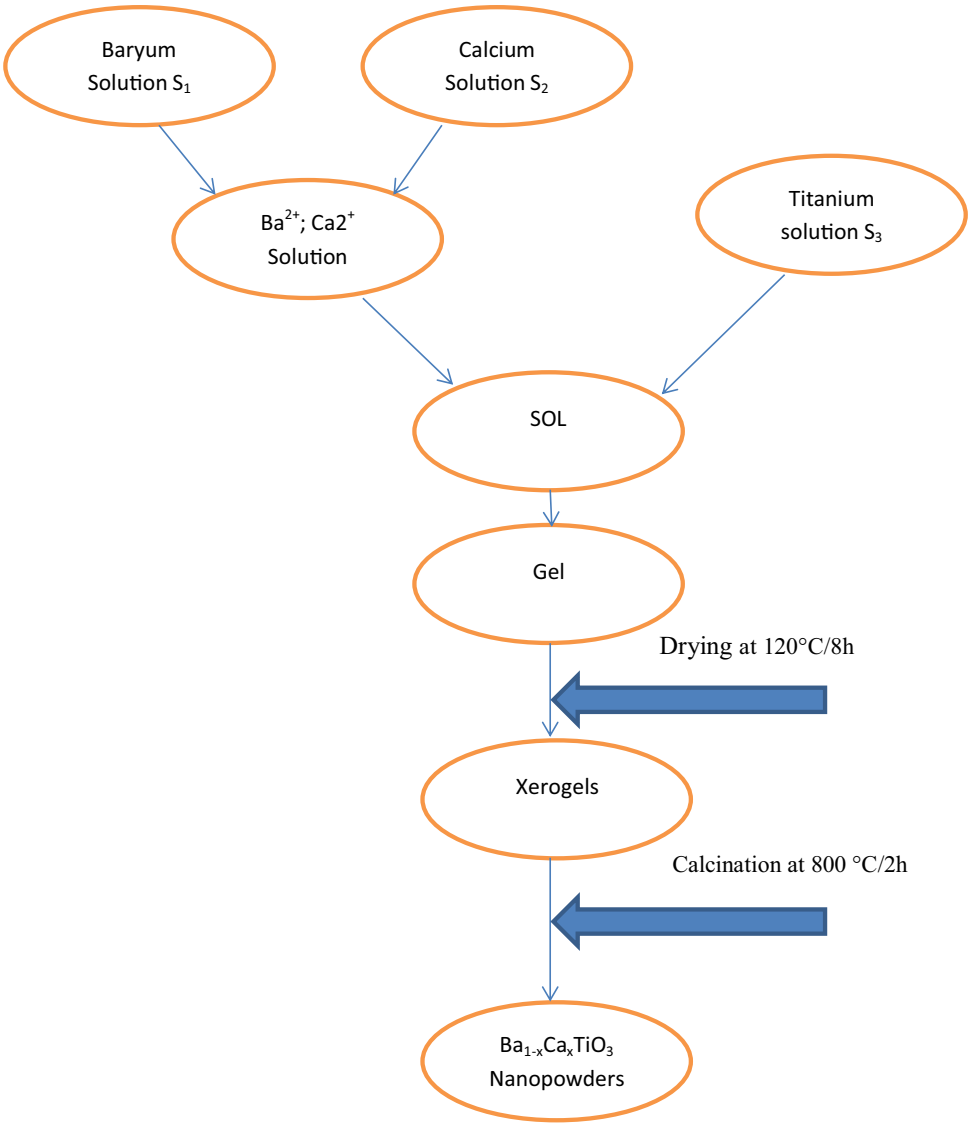

Fig. 1 Flow chart for the sol gel synthesis of Ba_{1-x} Ca_xTiO_3 nanopowders

3 Results and discussion

3.1 Thermal behaviour of $Ba_{0.9}Ca_{0.1}TiO_3$

In Fig. 2a, the thermogravimetric analysis (TGA) curve is shown, as recorded for the thermal decomposition process of the $Ba_{0.9}Ca_{0.1}TiO_3$ xerogel. The curve shows the xerogel mass loss of 37% (from 100 to 63%). In general, the decomposition process of $Ba_{0.9}Ca_{0.1}TiO_3$ xerogel proceeds in three steps: (1) a mass loss occurring between 40 and 250 °C and indicative of an existing solvent residue into the Xerogel (organic solvent and water); (2) a second mass loss is obvious between 250 and 400 °C, corresponding to the titanium butoxide decomposition to TiO_2, barium acetate to $BaCO_3$ and calcium acetate to $CaCO_3$ [15, 16]; and (3) a last mass loss occurring between 600 and 750 °C, attributed to the formation of $Ba_{0.9}Ca_{0.1}TiO_3$, which is created by the reaction between nanocrystalline carbonates ($BaCO_3$ and $CaCO_3$) and amorphous TiO_2, as well as the release of CO_2 [17].

Figure 2b shows the differential scanning calorimetry (DSC) curve recorded for the thermal decomposition process of $Ba_{0.9}Ca_{0.1}TiO_3$ xerogel, which confirms the results obtained by TGA. The peak at about 80 °C proves the evaporation of adsorbed moisture and volatile organic components of the xerogel, such as acetic acid and ethanol. In addition, there is another peak at 330 °C accredited to the decomposition of barium acetate, calcium acetate and tetrabutyl titanium to $BaCO_3$, $CaCO_3$ and TiO_2, respectively.

3.2 Phase and microstructure of the $Ba_{1-x}Ca_xTiO_3$ nanopowders

The X-ray diffraction (XRD) patterns of the $Ba_{1-x}Ca_xTiO_3$ nanopowders calcined at 800 °C for 2 h are shown in Fig. 3.

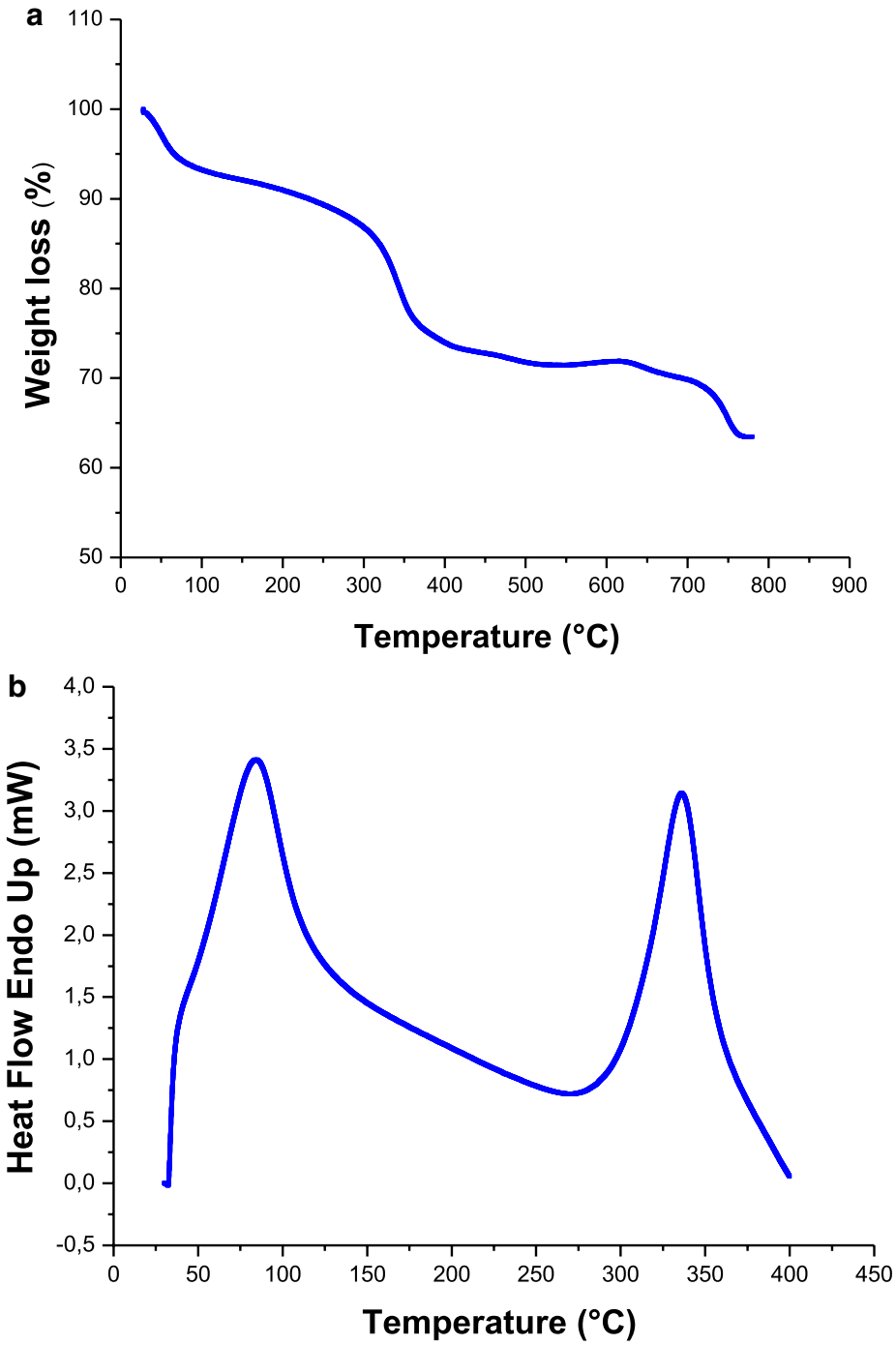

Fig. 2 **a** TG/**b** DSC patterns of $Ba_{1-x}Ca_xTiO_3$ xerogels

All the samples were well crystallized into a perovskite phase with a tetragonal structure (Fig. 3, JPCDS 83-1878) [18]. Besides, the orthorhombic phase of barium carbonate ($BaCO_3$, JCPDS 1-506) was detected with characteristic diffraction peaks at 24.08° and 34.28° (2θ) [18]. According to many previous works [19, 20], this small amount of $BaCO_3$ did not affect the formation of the perovskite phase of BCT. This shows the importance of this method, which drastically reduces the calcination time and temperature compared to the conventional solid-state reaction [11, 21–23].

A deep examination of the XRD patterns reveals that the diffraction peaks tend to shift to the higher degrees with the Ca content increase. This shows a good diffusion of Ca^{2+} in the $BaTiO_3$ host network [24, 25]. This is shown by the variation of the peak (200/220) at $2\theta = 45.5°$ (Fig. 3a, inset). It could be suggested that the substitution of Ba^{2+} ions (ionic radius 1.61 Å) by Ca^{2+} ions (ionic radius 1.34 Å)

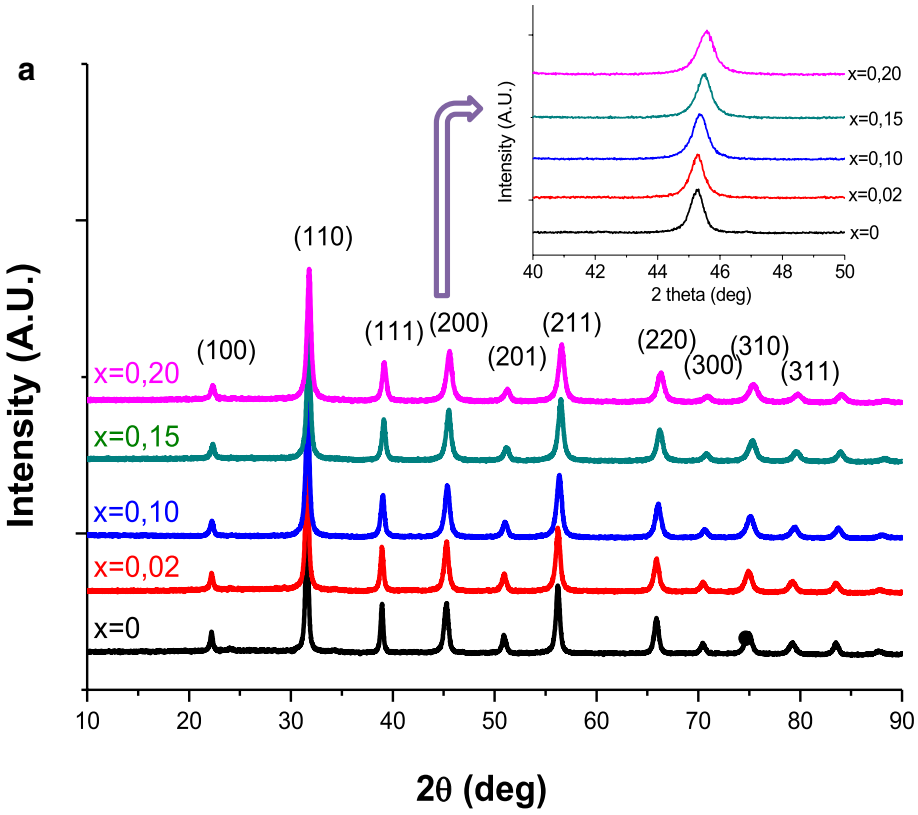

Fig. 3 **a** XRD patterns of $Ba_{1-x}Ca_xTiO_3$ nanopowders calcined at 800 °C for 2 h. The inset presents a zoom of (200) peak. **b** Rietveld analysis results of XRD patterns for $Ba_{1-x}Ca_xTiO_3$: experimental, calculated, and difference with $x = 0$, 0.05, 0.1, 0.15 and 0.2

promotes the lattice contraction and indicates the increase of the material pressure as well as the peaks broadening following the creation of stacking defects [24, 25]. The cell parameters were obtained by Rietveld refinement of XRD patterns using Fullprof program (Fig. 3b; Table 1). According to Jabarov et al. [26], under normal conditions, $BaTiO_3$ is in ferroelectric state up to the phase-transition temperature T_C, and the crystal structure is characterized by the tetragonal symmetry in space group P4mm with the unit cell parameters $a = b = 3.992 \pm 0.001$ Å, $c = 4.035 \pm 0.001$ Å (the tetragonal-distortion value $c/a = 1.011$). In our BT compound, the unit cell parameters are $a = b = 4.007 \pm 0.007$ Å, $c = 4.022 \pm 0.003$ Å, and thus the tetragonal-distortion value is c/a = 1.004. The difference could be attributed to the difference of the synthesis conditions.

Moreover, when the Ca^{2+} calcium ions replace those of Ba^{2+} in the $Ba_{1-x}Ca_xTiO_3$ network, the unit cell volume, as well as the lattice parameters (a, c), decreases (Table 1; Fig. 4a, b), which is due to the smaller ionic size of Ca^{2+} compared to that of Ba^{2+}. The partial substitution of Ba^{2+} by Ca^{2+} ions the $BaTiO_3$ lattice certainly causes local distortions in the tetragonal network which leads to the increasing of Coulomb interaction owing to the contraction of the Ti-O distance [27]. The literature shows that large ions are energetically favorable for doping with compensation for the vacancy charge, while smaller ions can self-compensate during replacement, such as Ba/Ca [28].

Using the Scherrer equation (Eq. 1), we can see that the average crystallite size of the BCT powders decreases with Ca content increase (Fig. 4c), such as for $x = 0$, 0.02, 0.05, 0.10, we have 25.04, 23.97, 22.44, 19.89 nm, respectively (Table 2).

The Scherrer equation is defined as:

$$L = K\lambda/(\beta \cos\theta), \quad (1)$$

where L, λ, K and β are defined as follows: L is the crystallite size; λ is the wavelength of the X-ray radiation ($\lambda = 1.54178$ Å) for $CuK_{\alpha 1}$; K is usually taken as 0.89; β is the line width at half-maximum height after correction of the equipment broadening.

As can be seen in Fig. 5a, the Scanning Electron Microscopy (SEM) photograph of the $Ba_{0.98}Ca_{0.02}TiO_3$ ($x = 0.02$) nanopowders calcined at 800 °C shows many nanoparticles that appear mostly in a round shape, having a large specific surface with the tendency to agglomerate [29]. The average particle size in the powders is ~ 81 nm, which is a little larger than that estimated by XRD analysis.

Figure 5b shows the SEM micrographs of the BCT ceramics sintered at 1200 °C for 4 h. It can be seen that the average grain size of $BaTiO_3$ ceramics decreases with the increase in Ca^{2+} content. The average grain size of $BaTiO_3$ is about

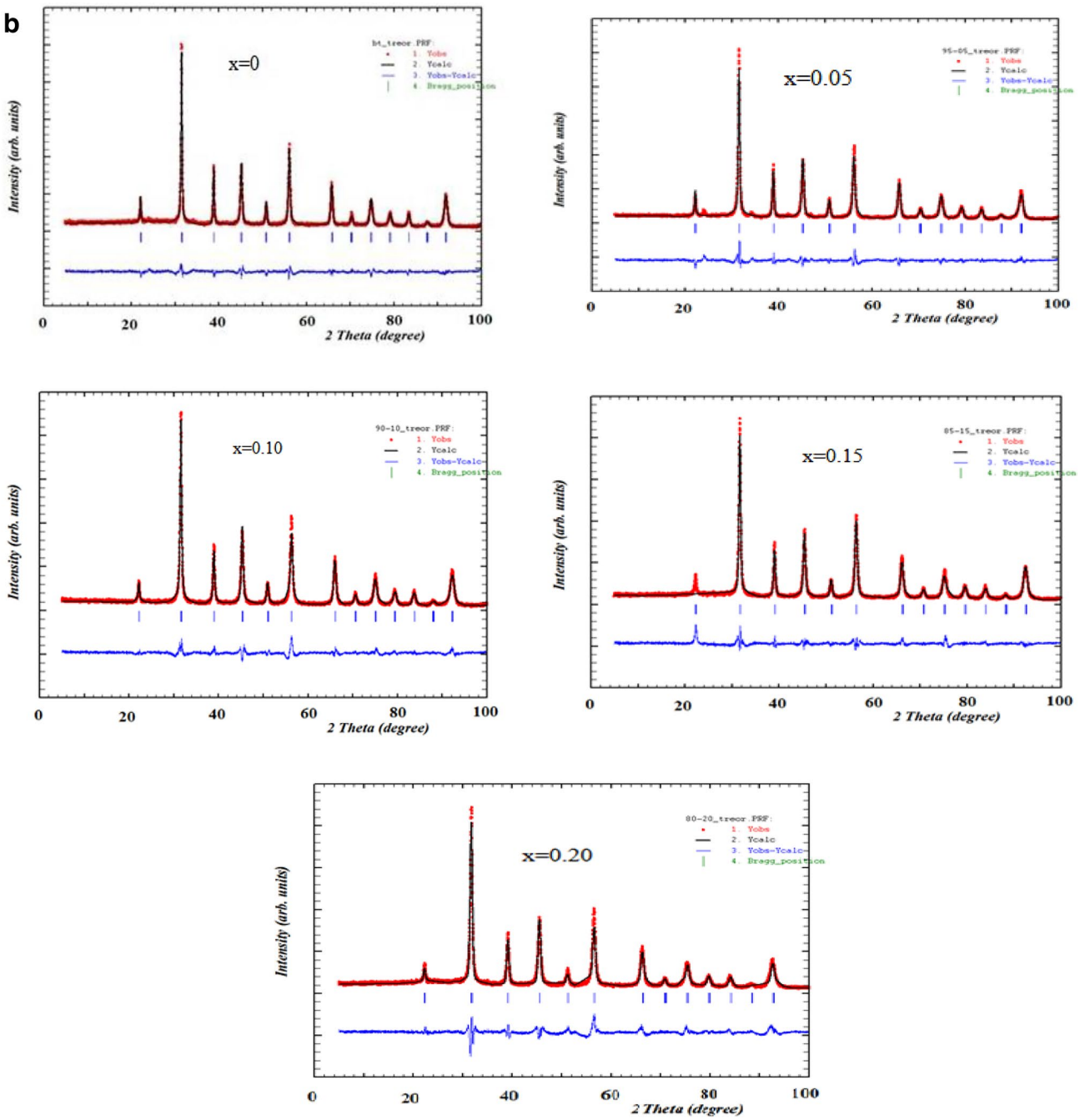

Fig. 3 (continued)

655 nm, whereas it is about 605 nm and 255 nm for $BaTiO_3$ with 3% and 5% of Ca^{2+}, respectively (Table 3). This indicates that the incorporation of Ca^{2+} inhibits the grain growth in $BaTiO_3$ ceramics which confirms the decreasing of the *c*/*a* ratio deduced by X-ray analysis. This result could be contributed to the substitution of larger Ba^{2+} ions by smaller Ca^{2+} ions, structural defects or agglomerate formation.

3.3 Raman spectroscopy

The Raman spectra of $Ba_{1-x}Ca_xTiO_3$ nanopowders calcined at 800 °C for 2 h are shown in Fig. 6. All the samples exhibit bands at around 183, 252, 305, 519 and 712 cm^{-1}, which defines a perovskite structure [30–32].

In fact, the crystallography shows that $BaTiO_3$ presents the following Raman-active modes: 4E (TO + LO) + 3 A_1

Table 1 Results of Rietveld refinement of X-ray diffraction data of $Ba_{1-x}Ca_xTiO_3$ measured at room temperature for the tetragonal region with space group P4mm for $x=0$, 0.05, 0.1, 0.15, and 0.2

Sample (x)	Space group	Cell parameters	R-factor
0	P4mm	a = b = 4.007(7) Å c = 4.022(3) Å v = 64.604(8) Å^3 c/a = 1.004(8)	R_p=25.9 R_{wp}=21.6 R_{exp}=13.22 χ^2=2.68
0.05	P4mm	a = b = 4.001(7) Å c = 4.014(0) Å v = 64.280(3) Å^3 c/a = 1.003(0)	R_p=25.7 R_{wp}=22.5 R_{exp}=12.47 χ^2=3.25
0.10	P4mm	*a* = *b* = 3.994(3) Å *c* = 4.005(7) Å *v* = 63.912(4) Å^3 *c*/*a* = 1.002(8)	R_p=26.0 R_{wp}=22.9 R_{exp}=12.49 χ^2=3.35
0.15	P4mm	*a* = *b* = 3.985(9) Å *c* = 3.996(7) Å *v* = 63.497(1) Å^3 *c*/*a* = 1.002(7)	R_p=27.2 R_{wp}=24.7 R_{exp}=12.91 χ^2=3.65
0.20	P4mm	*a* = *b* = 3.978(1) Å *c* = 3.987(0) Å *v* = 63.095 (3) Å^3 *c*/*a* = 1.002(2)	R_p=38.5 R_{wp}=29.3 R_{exp}=13.16 χ^2=4.06

(TO + LO) + B_1 (TO + LO) defining the tetragonal phase (space group P4mm). Indeed, Busca et al. [33] assigned peaks at 183, 252 and 519 cm^{-1} to three TO modes of A_1 symmetry i.e. to A_1 (TO_1), A_1 (TO_2) and A_1 (TO_3) modes, respectively.

Some authors (i.e. Smith et al.; Rabuffetti and Brutchey; Sun et al.) [34–36] have confirmed the fact that the combination of modes E (TO + LO) influences the formation of the mode at 305 cm^{-1}, which could be indicative of a displacement of Ti atoms from octahedral TiO_6. This suggests the intrinsic structural distortion in tetragonal $BaTiO_3$ [34].

For $BaTiO_3$ (i.e. $x=0$), the bands are observed at 518 and 712 cm^{-1}, whereas for $x=0.1$, they are observed at 519 and 715 cm^{-1}. Such displacement towards higher wavenumbers is due to Ba substitution by Ca in $BaTiO_3$, which leads to the formation of Ca_{Ba} defects. These two vibration modes are associated with those of the Ba–O bonds [30].

On the other hand, a shift was observed towards lower wavenumbers by increasing Ca content. While the bands are observed at 252 and 305 cm^{-1} for $x=0$, they are observed at 250 and 300 cm^{-1} for $x=0.1$. These two vibration modes are attributed to the vibrations of the Ti–O bonds [30, 34].

Moreover, in the Raman spectra, it is obvious that with Ca doping, the intensity proceeds first with an increase, then, followed by a decrease for all modes. In addition, the calcium incorporation into $BaTiO_3$ provokes the enlargement of some Raman bands corresponding to A_1 (TO) mode accompanied by an intensity decrease of B_1 + E (LO + TO) modes, which is the consequence of the disordered nature of the phase. When Ba is substituted by Ca, the electrical neutrality is normal.

Among others, the characteristic band intensity of the tetragonal phase at around 712 cm^{-1} is greatly decreased when x increases, indicating the lattice distortion and the tendency to transit from tetragonal to cubic phase. The results were confirmed by the XRD data.

3.4 FT-IR spectra analysis

Figure 7 shows the infra-red spectra of $Ba_{1-x}Ca_xTiO_3$ ($x=0.01$; 0.02; 0.03) calcined at 800 °C for 2 h, as recorded in the wavelength range from 400 to 4000 cm^{-1}.

The spectrum of pure BT nanopowder calcined at 800 °C shows almost total absence of absorption bands for organic compounds, such as the two absorption bands located at 1537 and 1392 cm^{-1}. These bonds are due to the symmetrical and asymmetric vibrations of the acetate groups present in the precursors used in synthesis.

A broad band is observed at 673 cm^{-1} that is a characteristic of crystalline $BaTiO_3$, indicating the oxygen-metal vibration of TiO_6 octahedra. It is attributed to the symmetric and asymmetric stretching of the Ti–O octahedron within [TiO_6], featuring its distortion [37].

The IR spectra of the $Ba_{1-x}Ca_xTiO_3$ nanopowders calcined at 800 °C ($x=0.01$; 0.02; 0.03) are similar to the spectrum of pure BT calcined at 800 °C. Indeed, the absence of bands of water and organic elements such as acetates clearly show that $Ba_{1-x}Ca_xTiO_3$ are well crystallized. In 1050–1200 cm^{-1} band region, the absorption peaks are attributed to CO_3^{2-} anions [38–40].

3.5 Photoluminescence (PL)

The photoluminescence spectra of the $Ba_{1-x}Ca_xTiO_3$ samples are shown in Figure 8. Photoluminescence in titanates may be due to radiative recombination between excited electrons and holes trapped in the states in the forbidden band of the perovskite, which is generated by oxygen deficiency and local distortions that behave as intrinsic defects due to the stretching of the Ti–O bond [18, 41]. In all cases, photoluminescence, therefore, depends on the structural and electronic properties including the presence of impurities and defects. The variation in Ca concentration has an effect on the emission process with a displacement in the peak position towards higher wavelengths (532.6 nm at $x=0$ to 534.8 nm at $x=0.1$), i.e. as Ca content increases, this redshift means the hole trapped states move upward to CB, which decreases the forbidden band gap (E_g) as observed in the PL spectra (Fig. 8).

The oxygen vacancies in titanates can occur in three different states of charge [42].

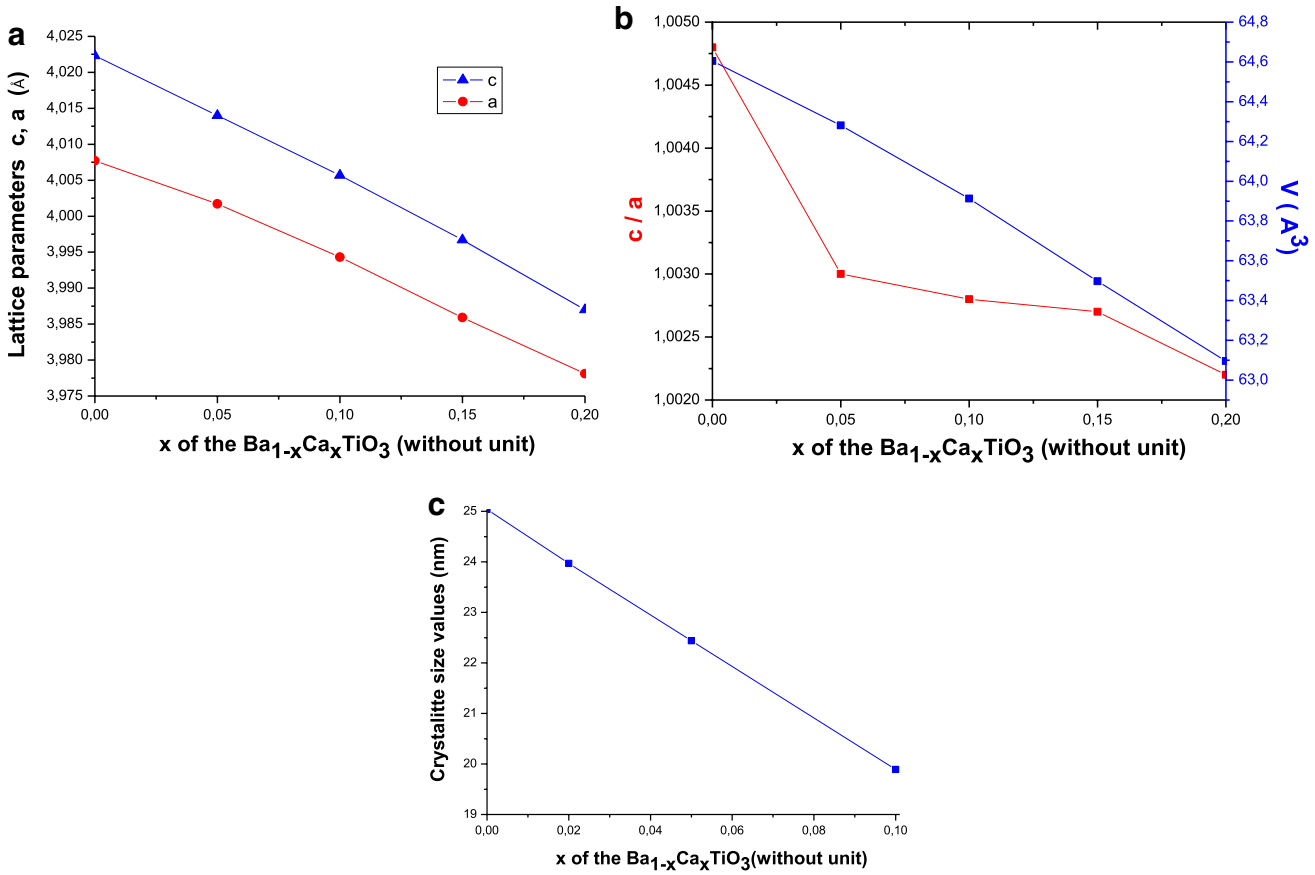

Fig. 4 **a** Plots of lattice parameters (*a, c*) variations with *x* for the $Ba_{1-x}Ca_xTiO_3$ nanopowders. **b** Plots of lattice parameters ratio *c*/*a* and unit cell volume *V* variations with *x* for the $Ba_{1-x}Ca_xTiO_3$ nanopowders. **c** Plots of crystallite size values variations with *x* for the $Ba_{1-x}Ca_xTiO_3$ nanopowders

Table 2 Average crystallite size values of the $Ba_{1-x}Ca_xTiO_3$ nanopowders

x	Crystallite size values (nm)
0	25.04
0.02	23.97
0.05	22.44
0.10	19.89

- Complex state $[TiO_5.V_o^x]$that has two paired electrons and is relatively neutral to the lattice.
- The only ionized complex state $[TiO_5.V_o^{\cdot}]$ with an unpaired electron.
- The doubly positively charged complex state $[TiO_5.V_o^{\cdot\cdot}]$ that did not trap any electron.

Before donor excitation, a hole in the acceptor and an electron in the donor are created, according to equations using the Kröger–Vink notations [43]:

$$\left[TiO_6\right]^x + \left[TiO_5 \cdot V_o^x\right] \rightarrow [TiO_6]' + [TiO_5.V_o^{\cdot}], \quad (2)$$

$$\left[TiO_6\right]^x + \left[TiO_5 \cdot V_o^{\cdot}\right] \rightarrow [TiO_6]' + [TiO_5 \cdot V_o^{\cdot\cdot}], \quad (3)$$

$$\left[TiO_5 \cdot V_o^{\cdot\cdot}\right] + {}^1\!/\!_2(O_2) \rightarrow \left[TiO_6\right], \quad (4)$$

where $[TiO_6]'$ is donor, $[TiO_5{\cdot}V_o^{\cdot}]$ is donor–acceptor and $[TiO_5{\cdot}V_o^{\cdot\cdot}]$ is acceptor.

Thus, it is likely that the addition of Ca contributes to the formation of deformed groups or to the broken symmetry of the resulting complex group (containing gaps).

3.6 Dielectric properties

As the dielectric response for powders treated at 800 °C is very low (the dielectric permittivity did not exceed 280) (Fig. 9), it is of no interest for the present study. That is why it was necessary to pass to a higher sintering temperature optimized at 1200 °C, which leads to an increase of the specific surface causing the boost of the polarizability and thus obtaining a considerable dielectric response.

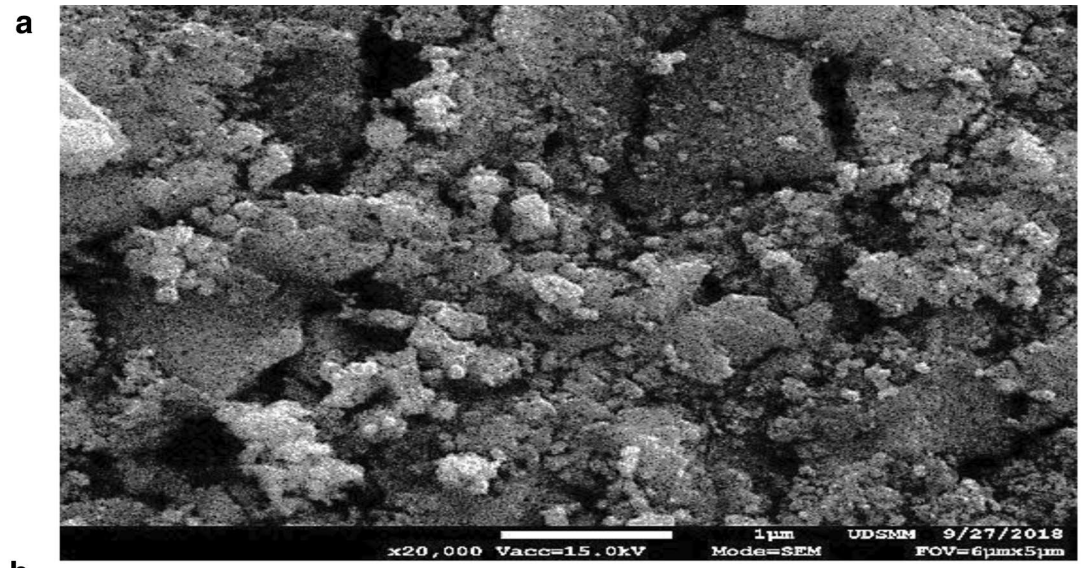

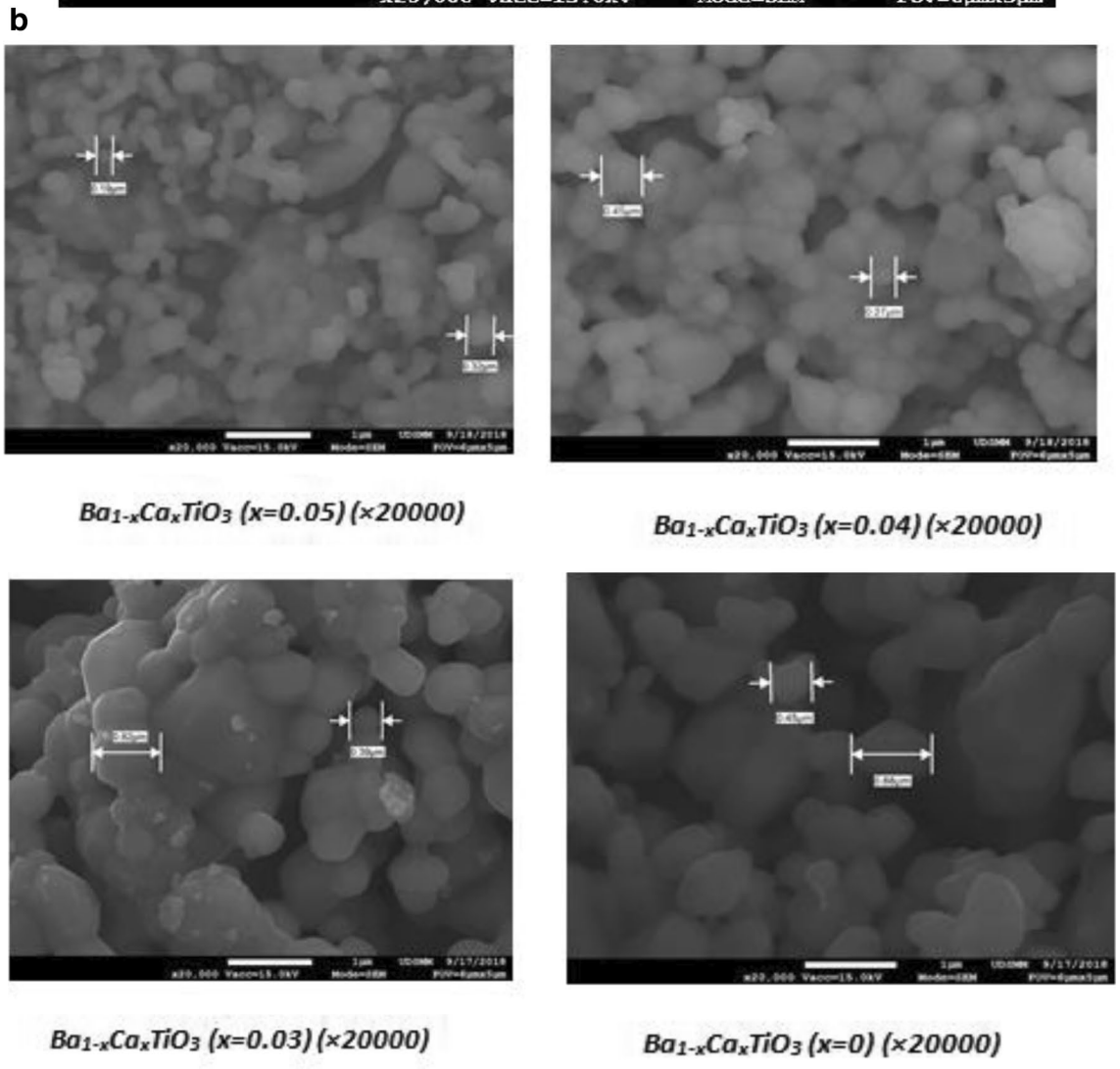

Fig. 5 **a** Scanning electron microscopy (SEM) micrograph of the $BaTiO_3$ nanopowder calcined at 800 °C for 2 h. **b** Scanning electron microscopy (SEM) micrographs of the $Ba_{1-x}Ca_xTiO_3$ ceramics sintered at 1200 °C for 4 h

Table 3 Average crystallite size values of the $Ba_{1-x}Ca_xTiO_3$ ceramics

x	Crystallite size values (nm)
0	655
0.03	605
0.04	360
0.05	255

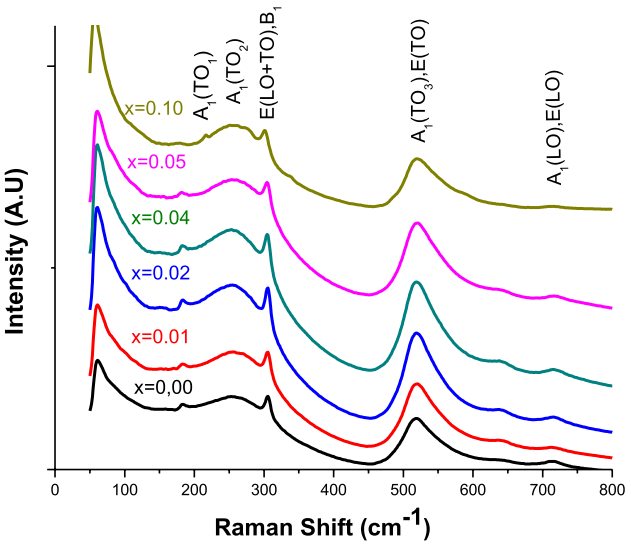

Fig. 6 Raman spectra of $Ba_{1-x}Ca_xTiO_3$ nanopowders calcined at 800 °C for 2 h

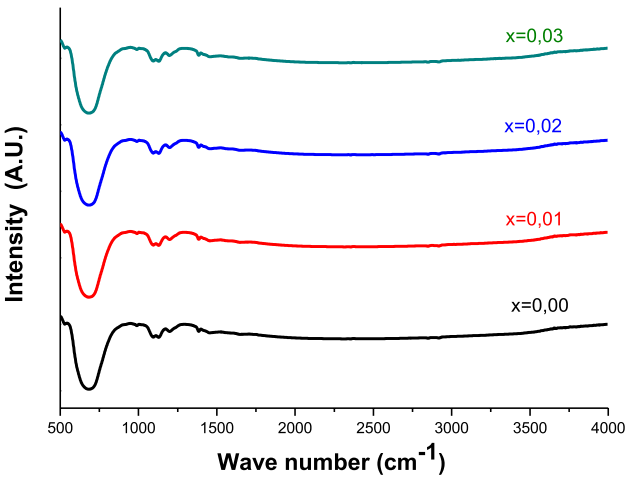

Fig. 7 FT-IR spectra of $Ba_{1-x}Ca_xTiO_3$

Nevertheless, it can be mentioned that the value of dielectric constants of the nanopowders calcined at 800 °C vary slightly over the temperature range on either side of room temperature, therefore, making this type of material a potential candidate for the manufacture of capacitors at nanoscale (Fig. 9).

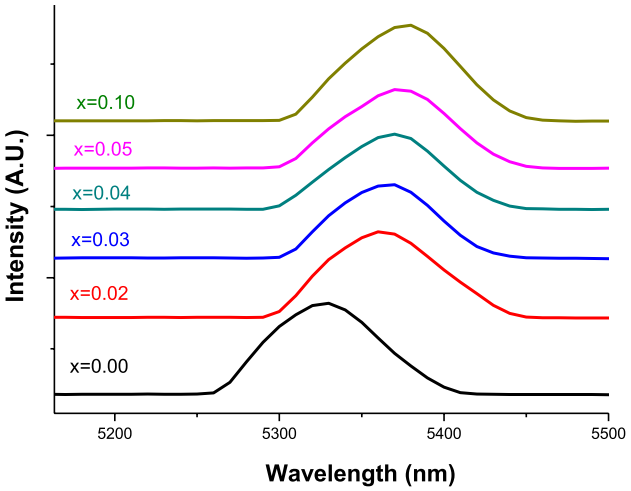

Fig. 8 Photoluminescence spectra of the $Ba_{1-x}Ca_xTiO_3$

As shown in Fig. 10, the Curie temperatures T_C were detected at 403.46 ± 0.05 K (130.46 °C) for $BaTiO_3$, 413.28 ± 0.05 K (140.28 °C) for $Ba_{0.96}Ca_{0.04}TiO_3$, 416.91 ± 0.05 K (143.91 °C) for $Ba_{0.95}Ca_{0.05}TiO_3$ and 414.53 ± 0.05 K (141.53 °C) for $Ba_{0.90}Ca_{0.1}TiO_3$ (Fig. 10; Table 4). Moreover, the value of Curie Weiss constant C_W varied with the increase of Ca^{2+} concentration. On the other hand, we can see that orthorhombic—tetragonal transition temperatures shifted to the lower ones (Fig. 10; Table 4).

The dielectric constant ε_r and the Curie Weiss temperature of a ferroelectric can be described by Curie Weiss's law (Eq. 5):

$$\varepsilon_r = C_w/(T - T_0) \text{ for } T > T_0, \quad (5)$$

where C_w is the Curie Weiss constant, T_0 is the Curie Weiss temperature.

The curves representing $1/\varepsilon_r$ as function of $\frac{T - T_0}{C_w}$ are shown in Fig. 10 (insets).

Figure 11 reveals the effect of calcium on Curie transition T_C which increased significantly between 0 and 5% of Ca^{2+}, then decreased slightly. On the other hand, $Ba_{0.96}Ca_{0.04}TiO_3$ presents the higher maximum permittivity value. For all Ca^{2+} concentration, it is clear that T_0 always remains lower than T_C; the nature of the transition is of the first order.

Initially, the dielectric constant ε_r increases gradually until reaching its maximum at Curie temperature T_C, and then an abrupt fall was observed at temperature above T_C, indicating a phase transition (Fig. 10). This leads to a phase transition occurring at (T_c), at which $Ba_{1-x}Ca_xTiO_3$ transformed from the ferroelectric phase (polarized state) into the

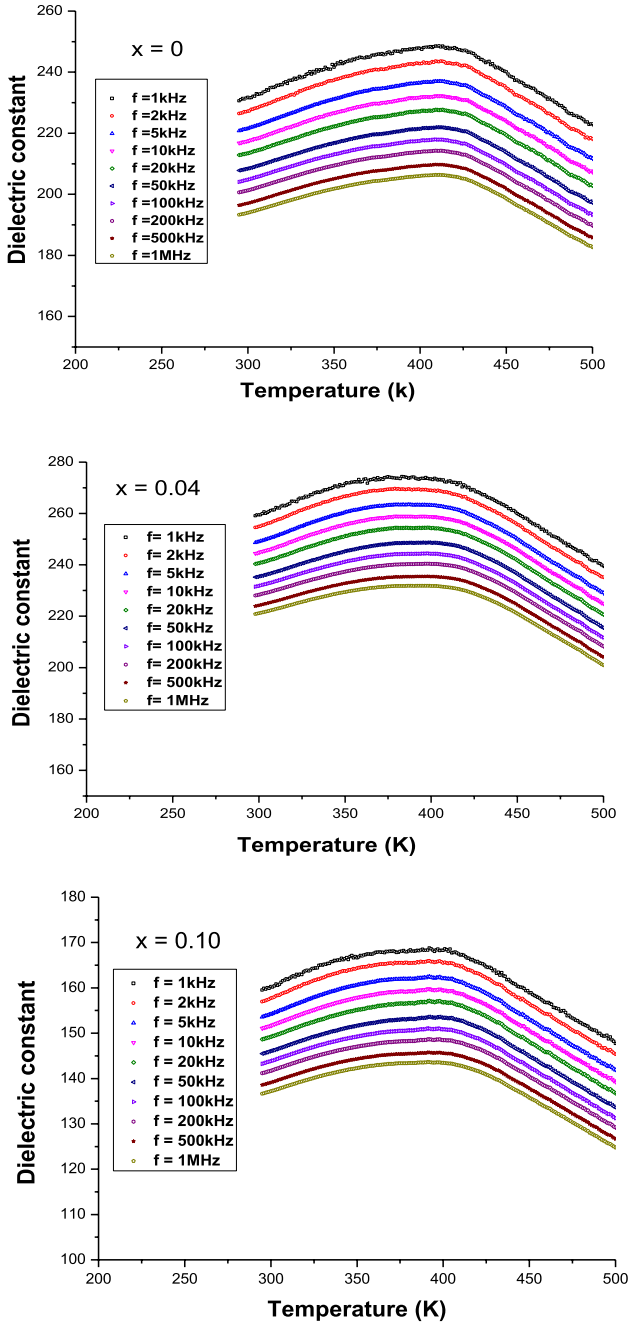

Fig. 9 Evolution of the dielectric constant of $Ba_{1-x}Ca_xTiO_3$ nanopowders calcined at 800 °C as a function of temperature

paraelectric phase (unpolarized state) [44]. In this process, the polarization affects the permanent dipole moment. Furthermore, the negatively charged O^{2-} and positively charged Ti^{4+} ions are displaced from their symmetrical positions, which are known as upward displacement [44].

In general, the distortion of the material along *c* axis can lead to a crystallization of tetragonal phase [45–47]. The dielectric behavior of barium calcium titanate produced in the tetragonal phase is in good agreement with our XRD data.

Alternatively, the dielectric constant ε_r has significantly decreased by conducting the heating of $Ba_{1-x}Ca_xTiO_3$ above its Curie temperature. This can be explained by the fact that the formed tetragonal phase (noncentrosymmetric) at lower temperature has been transformed into cubic phase (Centrosymmetric) at temperature higher than T_C [45]. Thus, the formed crystalline phase of $Ba_{1-x}Ca_xTiO_3$ is considered as paraelectric, which has no permanent dipole moment that explains its dielectric behavior [44].

4 Conclusion

The structural, spectroscopic and dielectric properties of $Ba_{1-x}Ca_xTiO_3$ (BCT where $x=0$–0.2) nanopowders prepared at low temperature of 800 °C by the recent sol–gel route have been investigated. The structural characterization of the BCT compounds by XRD reveals a complete crystallization in the pure perovskite structure with nanocrystalline sizes. This result was confirmed by the Raman spectroscopic analysis that exhibits bands at around 183, 252, 305, 519 and 712 cm^{-1}, which define a perovskite structure. The samples show single tetragonal phase in space group P4mm. Lattice parameters (*a, c*), unit cell volume and crystallite sizes were affected by Ca substitution in $BaTiO_3$ lattice due to the difference of atomic radii of calcium and barium.

The microstructure of $BaTiO_3$ calcined at 800 °C for 2 h shows that the distribution of the grains is rather uniform with an average diameter of 81 nm. The SEM data agreed with the results obtained by Scherrer equation using XRD patterns.

It was observed that the variation in Ca concentration promoted a red-shift in the PL peaks. These results prove the reduction of the optical band gap value by appearance of the inter-band electron levels. The specific surface would be determined by BET analysis. Nevertheless, in general and according to Dubois et al. [48], it is often assumed that there is an inverse proportionality between surface area and particle size, thus, as BCT was at nanoscale, its higher surface area leads to a high photoluminescence emission shown by this material, thus making it a good candidate for optical applications.

The dielectric properties of $Ba_{1-x}Ca_xTiO_3$ systems sintered at 1200 °C for 4 h in the ferroelectric phase showed strong temperature dependence. Therefore, the calcium substitution greatly affects Curie temperature T_C which increased significantly between 0 and 5% of Ca^{2+}, and then it decreased slightly up to 10%. Moreover, the value of Curie Weiss constant C_W varies according to Ca^{2+} concentration.

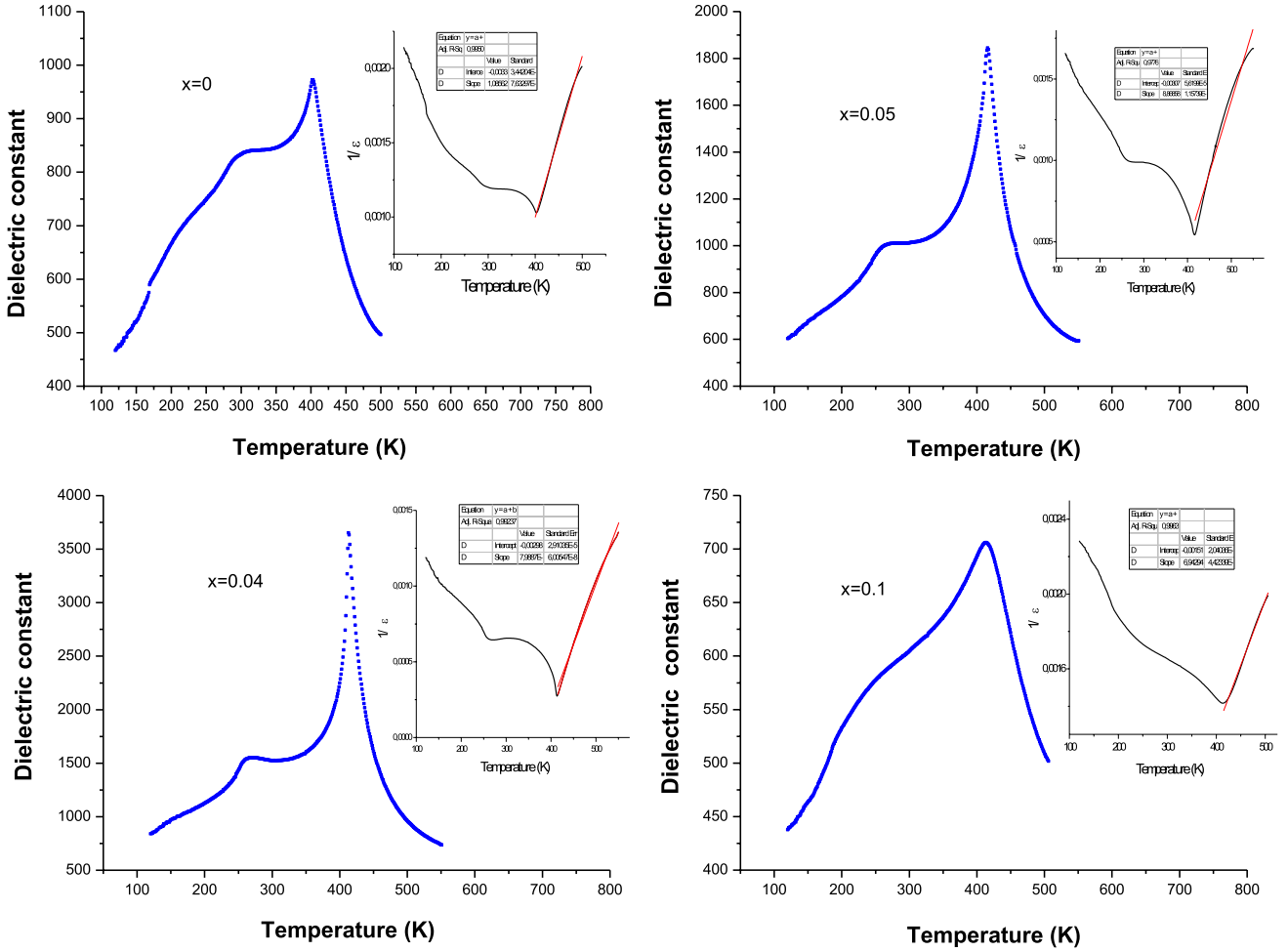

Fig. 10 Evolution of the dielectric constant of $Ba_{1-x}Ca_xTiO_3$ ceramics sintered at 1200 °C as a function of temperature. The insets present variations of the inverse of the dielectric constant of $Ba_{1-x}Ca_xTiO_3$ ceramics as a function of the temperature at $f = 1$ kHz

Table 4 Dielectric results for the $Ba_{1-x}Ca_xTiO_3$ ceramics sintered at 1200 °C at $f = 1$ kHz

x	ε_{max}	T_C (K)	T_0 (K)	C_W	$T_{ortho-Tetra}$ (K)
0	972.36	403.46	382.89	9.21 10^4	293.93
0.04	3644.42	413.28	373.20	12.51 10^4	260.90
0.05	1848.28	416.91	402.64	9.2410^4	250.20
0.10	706.21	414.53	398.04	14.40 10^4	216.36

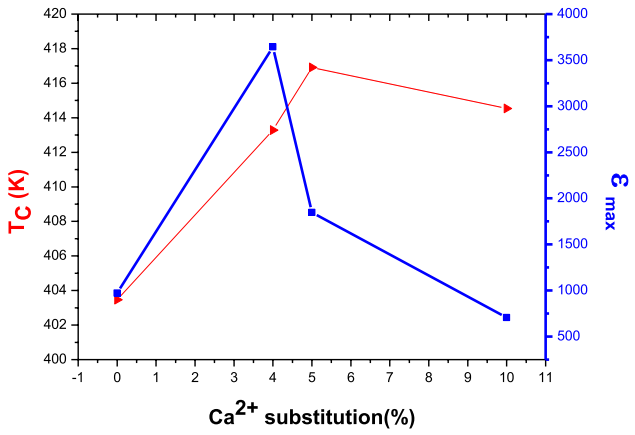

Fig. 11 Variation of Curie temperature and ε_{max} with calcium concentration x for the $Ba_{1-x}Ca_xTiO_3$ ceramics at $f = 1$ kHz

On the other hand, the concentration $x = 0.1$ shows the most diffuse transition character.

References

1. H.Y. Tian, Y. Wang, J. Miao, H.L.W. Chan, C.L. Choy, J. Alloys Compd. **431**, 197–202 (2007)
2. F. Boujelben, F. Bahri, C. Bouday, A. Maalej, H. Khemakhem, A. Simon, M. Maglione, J. Alloys Compd. **481**, 559–562 (2009)
3. Q. Xu, X.F. Zhang, Y.H. Huang, W. Chen, H.X. Liu, M. Chen, B.H. Kim, J. Alloys Compd. **488**, 448–453 (2009)
4. J.Y. Chen, Y.W. Tseng, C.L. Huang, J. Alloys Compd. **494**, 205–209 (2010)
5. X. Cheng, M. Shen, Solid State Commun. **141**, 587–590 (2007)
6. D. Fu, M. Itoh, S. Koshihara, Appl. Phys. Lett. **93**, 012904 (2008)
7. X. Cheng, M. Shen, Mater. Res. Bull. **42**, 1662–1668 (2007)
8. F.V. Motta, A.P.A. Marques, J.W.M. Espinosa, P.S. Pizani, E. Longo, J.A. Varela, Curr. Appl. Phys. **10**, 16–20 (2010)
9. S.V. Trukhanov, A.V. Trukhanov, S.G. Stepin, H. Szymczak, C.E. Botez, Phys. Solid State **50**, 886–893 (2008)
10. V.D. Araujo, F.V. Motta, A.P.A. Marques, C.A. Paskocimas, M.R.D. Bomio, E. Longo, J.A. Varela, J. Mater. Sci. **49**, 2875–2878 (2014)
11. S.V. Trukhanov, V.V. Fedotova, A.V. Trukhanov, S.G. Stepin, H. Szymczak, Crys. Rep. **53**, 1177–1180 (2008)
12. V.V. Atuchin, T.A. Gavrilova, J.-C. Grivel, V.G. Kesler, Surf. Sci. **602**, 3095–3099 (2008)
13. V.V. Atuchin, T.A. Gavrilova, J.-C. Grivel, V.G. Kesler, I.B. Troitskaia, J. Solid State Chem. **195**, 125–131 (2012)
14. H.P. Ji, L. Wang, M.S. Molokeev, N. Hirosaki, R.J. Xie, Z.H. Huang, Z.G. Xia, O.M.T. Kate, L.H. Liu, V.V. Atuchin, J. Mater. Chem. C **4**, 6855–6863 (2016)
15. B. Cui, P. Yu, X. Wang, J. Alloys Compd. **459**, 589–593 (2008)
16. F.V. Motta, A.P.A. Marques, C.A. Paskocimas, M.R.D. Bomio, A.S.F. Santos, E.R. Leite, J.A. Varela, E. Longo, in *Polymerization*, 3nd edn. (INTECH, Rijeka, 2012), pp. 261–278
17. Y.Y. Yao, J.N. Cheng, P. Zhao, J. Chin. Ceram. Soc. **32**, 751–754 (2004)
18. A.E. Souza, S.R. Teixeira, C.M. -Santos, W.H. Schreiner, P.N.L. Filho, E. Longo, J. Mater. Chem. C **2**, 7056 (2014)
19. R.S. Silva, M.I.B. Bernardi, A.C. Hernandes, J. Sol–Gel Sci. Technol. **42**, 173–179 (2007)
20. R.S. Silva, A.C. Hernandes, J.-C. M'Peko, Mater. Res. **15**, 522–529 (2012)
21. C.S. Lim, A.S. Aleksandrovsky, M.S. Molokeev, A.S. Oreshonkov, V.V. Atuchin, J. Solid State Chem. **228**, 160–166 (2015)
22. C.S. Lim, A.S. Aleksandrovsky, M.S. Molokeev, A.S. Oreshonkov, D.A. Ikonnikov, V.V. Atuchin, Dalton Trans. **45**, 15541–15551 (2016)
23. C.S. Lim, V.V. Atuchin, A.S. Aleksandrovsky, M.S. Molokeev, Mater. Lett. **181**, 38–41 (2016)
24. R.S. Silvaa, L.M. Jesus, T.C. Oliveira, D.V. Sampaio, J.C.A. Santos, A.C. Hernandes, J. Eur. Ceram. Soc. **36**, 4023–4030 (2016)
25. M.R. Panigrahi, S. Panigrahi, Phys. B **405**, 1787–1791 (2010)
26. S.H. Jabarov, A.I. Mammadov, A.V. Trukhanov, J. Surf. Invest. **11**, 223–225 (2017)
27. X. Jin, D. Sun, Y. Zhang, J. Qian, J. Electrocer. **22**, 285–290 (2009)
28. J.A. Dawson, X. Li, C.L. Freeman, J.H. Harding, D.C. Sinclair, J. Mater. Chem. C **1**, 1574–1582 (2013)
29. X.Y. Wang, B. Lee, M. Hu, E.A. Payzant, D.A. Blom, J. Eur. Ceram. Soc. **26**, 2319–2326 (2006)
30. A. Pinczuk, W. Tayler, E. Burstein, Solid state Commun. **5**, 429 (1967)
31. M. Didomenico, S.H. Wemple, S.P.S. Porto, Phys. Rev. **174**, 522–530 (1968)
32. Y. Shiratori, C. Pithan, J. Dornseiffer, R. Waser, J. Raman Spectrosc. **38**, 1288–1299 (2007)
33. G. Busca, V. Buscaglia, M. Leoni, P. Nanni, Chem. Mater. **6**, 955–961 (1994)
34. Q. Sun, Q. Gu, K. Zhu, R. Jin, J. Liu, J. Wang, J. Qiu, Sci. Rep. **7**, 42274 (2017)
35. M.B. Smith, K. Page, T. Siegrist, P.L. Redmond, E.C. Walter, R. Seshadri, L.E. Brus, M.L. Steigerwald, J. Am. Chem. Soc. **130**, 6955–6963 (2008)
36. F.A. Rabuffetti, R.L. Brutchey, J. Am. Chem. Soc. **134**, 9475–9487 (2012)
37. L. Wang, H. Kang, D. Xue, C. Liu, J. Crys. Growth **311**, 605–607 (2009)
38. Y.D. Hou, L. Hou, J.F. Yang, M.K. Zhu, H. Wang, H. Yan, Acta Chim. Sinica **10**, 950–954 (2007)
39. Y.V. Kolen'ko, K.A. Kovnir, I.S. Neira, T. Taniguchi, T. Ishigaki, T. Watanabe, N. Sakamoto, M. Yoshimura, J. Phys. Chem. C **111**, 7306–7318 (2007)
40. X.S. Wang, L.L. Zhang, H. Liu, J.W. Zhai, X. Yao, Mater. Chem. Phys. **112**, 675–678 (2008)
41. W.F. Zhang, Z. Yin, M.S. Zhang, Z.L. Du, W.C. Chen, J. Phys. Cond. Mater. **11**, 5655–5660 (1999)
42. K. Asokan, J.C. Jan, J.W. Chiou, W.F. Pong, P.K. Tseng, I.N. Lin, J. Synchrot. Radiat. **8**, 839–841 (2001)
43. F.A. Kröger, H.J. Vink, Solid State Phys. **3**, 307–435 (1956)
44. R.M. Mahani, I.K. Battisha, M. Aly, A.B. Abou-Hamad, J. Alloys Compd. **508**, 354–358 (2010)
45. M. Nayak, T.Y. Tseng, J. Thin Solid Films **408**, 194–199 (2002)
46. X. Wei, G. Xu, Z. Ren, Y. Wang, G. Shen, G. Han, Mater. Lett. **62**, 3666–3669 (2008)
47. I.K. Battisha, A.B. Abou Hamad, R.M. Mahani, Phys. B **404**, 2274–2279 (2009)
48. I.E. Dubois, S. Holgersson, S. Allard, M.E. Malmstrom, W.-R. Interaction, B. Torres-Alvarado (eds.), Taylor & Francis Group, London, 717–720 (2010)